

Unraveling dark Higgs mechanism via dark photon production at an e^+e^- collider

Song Li,^{1,*} Jin Min Yang,^{1,2,†} Mengchao Zhang,^{3,‡} Yang Zhang,^{1,§} and Rui Zhu^{2,4,¶}

¹*School of Physics, Henan Normal University, Xinxiang 453007, P. R. China*

²*Institute of Theoretical Physics, Chinese Academy of Sciences, Beijing 100190, P. R. China*

³*Department of Physics and Siyuan Laboratory,*

Jinan University, Guangzhou 510632, P. R. China

⁴*School of Physics, University of Chinese Academy of Sciences, Beijing 100049, P. R. China*

Abstract

In the phenomenology study of dark photon, its mass origin is usually not considered. But in the theory construction, its mass is often generated via a dark Higgs mechanism, which predicts a dark Higgs particle. In this work, we study the impact of such a light (non-decoupled) dark Higgs particle in the collider detection of the dark photon. Assuming both the dark photon and dark Higgs decay invisibly, the search for dark photon via its photon-associated production would be affected by the dark Higgs emission from the dark photon. To examine this effect, for the dark photon and dark Higgs not too light, the hard scattering process with one dark Higgs in the final-state is taken as the leading-order correction; while for their masses much lower than the collision energy, merging is performed in the dark sector to deal with infrared divergence. We find that the dark Higgs emission can affect the signal cross section and the kinematic variables such as the invisible mass. We recast the analysis from the BaBar collaboration and obtain a new exclusion limit for the invisible dark photon.

* chunglee@htu.edu.cn

† jmyang@itp.ac.cn

‡ Corresponding author, mczhang@jnu.edu.cn

§ yang.phy@foxmail.com

¶ Corresponding author, zhurui@itp.ac.cn

CONTENTS

I. Introduction	3
II. Final-state radiation (FSR) in the dark sector	4
A. The dark-sector model	4
B. Dark final-state radiation	5
C. Splitting functions for dark shower	6
III. Impact of the dark FSR	7
A. Increase in the dark photon production cross section	7
B. Flattening of the squared missing mass distribution	9
IV. Recasting BaBar analysis with dark FSR effects	11
A. Decompose the impact	11
B. Effect of signal distribution	12
C. Effect of cross section	13
D. New limit on the mixing parameter	14
V. Conclusion	15
Acknowledgments	16
A. Derivation of splitting functions	16
1. Feynman rules	16
2. Kinematics	17
3. Results of the calculation	18
References	18

I INTRODUCTION

The existence of dark matter (DM) has been confirmed through its gravitational effects. However, its non-gravitational interactions have not been experimentally detected to date. The null result of DM detection indicates that the interaction between DM and the Standard Model (SM) particles may be very weak, which also largely excludes the natural parameter space of common WIMP (Weakly Interacting Massive Particle) models [1–7]. In recent years, an increasing number of studies have shifted focus to investigating the so-called “dark sector” models. In such models, the DM generally couples to SM particles via a vector particle called dark photon (DP, labeled by A') through a small kinetic mixing between DP and the SM photon [8–18], and thus make it easier to escape the limits on WIMPs. Consequently, experimental searches for these dark sector models often focus on the detection of DP. The DP couples with the SM charged particles via a kinetic mixing, and thus can be detected by multiple experiments like beam-dump experiments [19], low energy electron-positron colliders [20–23], fixed target experiments [24–28], or forward detectors [29–31]. Current data already excluded a large region in the 2-dimensional parameter space $(m_{A'}, \varepsilon)$, with $m_{A'}$ being the DP mass and ε the kinetic mixing parameter [32–46].

However, the detection of DP only based on $m_{A'}$ and ε might be oversimplified. It is generally considered that the DP mass $m_{A'}$ is from the Stueckelberg mechanism. But Stueckelberg mechanism is only valid when the dark Higgs (labeled by s) is much heavier than the DP, i.e. $\lambda \gg g'$, with λ and g' being the dark Higgs self-coupling and the dark $U(1)'$ gauge coupling, respectively. Due to the perturbative unitarity bound [47, 48], λ should be smaller than 4π [49]. And g' is generally not too small in some model setting [15, 50–53]. So, $\lambda \gg g'$ is generally invalid and we can not treat dark Higgs to be decoupled.

There are already some studies in the literature that study the DP and dark Higgs in collider detection simultaneously [54–59]. All of these studies rely on the assumption that DP decays mainly to lepton pair or charged mesons, i.e. they only consider visible DP. Furthermore, most of these studies are considering dark Higgsstrahlung process $e^+e^- \rightarrow A's$ at electron-positron colliders. Different from previous studies, in this work we analyze the case where both the DP and the dark Higgs are invisible. Certainly in this invisible case the dark Higgsstrahlung process $e^+e^- \rightarrow A's$ can not be used to search for the dark sector, because all the final state particles would not leave any trace in the detector in this case. Instead, we consider the process $e^+e^- \rightarrow \gamma A's$ and it contains an extra dark Higgs in the final state coming from the dark final-state radiation (FSR) process $A' \rightarrow A's$.

For the invisible dark DP detection at colliders, the missing mass square M_X^2 is a typical kinematical variable. We will show that the dark FSR process $A' \rightarrow A's$ changes the distribution of M_X^2 . Furthermore, when the center-of-mass collision energy \sqrt{s} is much larger than $m_{A'}$ and m_s , the collinear divergence would appear in the fixed-order perturbative calculation. This problem can be solved by the “dark shower” method [60–63], which is similar to the familiar parton shower in the SM. By merging the contribution from dark shower and fixed-order dark radiation process,

we obtain a reliable description of the dark FSR process $e^+e^- \rightarrow \gamma A's$. A case study at BaBar is given to show how does the dark FSR process change the search limit of DP.

In the next section we briefly introduce the model in this study, and delineate how to characterize final-state radiation in the dark sector. In Section III, we formally analyze the potential impact of the dark FSR both on the cross section and on the distribution of the missing mass square. As a case study, in Section IV, concentrating on the BaBar collaboration's search for invisible dark photon, we quantitatively examine the effect of the dark FSR on the exclusion limit. This work is concluded in Section V.

II FINAL-STATE RADIATION (FSR) IN THE DARK SECTOR

A The dark-sector model

The dark sector in this work is charged under a dark $U(1)'$ gauge which is spontaneously broken via a dark Higgs mechanism. The complete Lagrangian for the dark sector before symmetry breaking is (diag(+, -, -, -) metric):

$$\mathcal{L}_{\text{dark}} = (D_\mu S)^\dagger D^\mu S - \frac{1}{4} F'_{\mu\nu} F'^{\mu\nu} + \mu^2 S^\dagger S - \frac{1}{4} \lambda (S^\dagger S)^2 + \bar{\chi} (i\not{D} - m_\chi) \chi - \varepsilon e J_\mu^{\text{EM}} A'^\mu \quad (1)$$

where S is the complex dark Higgs field before symmetry breaking, $D_\mu = \partial_\mu - ig' A'_\mu$ is the covariant derivative (g' is the dark gauge coupling), $F'_{\mu\nu} = \partial_\mu A'_\nu - \partial_\nu A'_\mu$ is the field strength of DP A' . A light dark fermion χ is introduced to make DP decay invisibly. In the last term, J_μ^{EM} is the SM electromagnetic current, ε and e are the kinetic mixing parameter and electric charge, respectively.

After symmetry breaking, the dark Higgs field obtains a vacuum expectation value (VEV) $v = 2\mu/\sqrt{\lambda}$ and can be decomposed as $S = \frac{1}{\sqrt{2}}(v + s + ia)$. The masses of dark Higgs s and dark photon A' are given by

$$m_s^2 = \frac{1}{2} \lambda v^2, \quad m_{A'}^2 = g'^2 v^2. \quad (2)$$

To simplify our analysis, in the rest of this paper we assume $m_s = m_{A'}$. The mass of dark fermion χ is simply taken to be much smaller than $m_{A'}$, which makes the invisible decay channel $A' \rightarrow \bar{\chi}\chi$ to be dominant. We further assume the coupling of Higgs portal $(S^\dagger S)(H^\dagger H)$ (H is the SM Higgs doublet) to be negligible, and thus the dark Higgs s can only decay via off-shell dark photons ($s \rightarrow A'^* A'^* \rightarrow \bar{\chi}\chi\bar{\chi}\chi$) which also makes the dark Higgs invisible.

Compared with the conventional DP model with 2 input parameters $\{\varepsilon, m_{A'}\}$, our dark Higgs model has 3 input parameters $\{\varepsilon, m_{A'} (= m_s), \alpha'\}$. Here $\alpha' = g'^2/4\pi$ is the dark fine structure constant.

B Dark final-state radiation

The DP can be generated by high energy charged particles via the kinetic mixing. Because the mixing parameter ε is very small, we consider the process with only one DP in the final state. In our dark sector model with a Higgs mechanism, there are 3-point couplings between dark Higgs and DP, such as $A'_\mu A'^\mu s$ and $A'^\mu (a \overleftrightarrow{\partial}_\mu s)$. So it is possible for a final-state DP to emit a dark Higgs if α' is not too small. This dark Higgs emitting process, $A' \rightarrow A's$, will be called the dark final-state radiation (FSR) in the rest of this paper.

To deal with the dark FSR, we adopt the method as illustrated in the diagrammatic sketch Fig. 1. Comparing to the center-of-mass energy \sqrt{s} for a certain collider, if $(m_{A'} + m_s)$ is not too small, the fixed-order calculation is valid. But when $(m_{A'} + m_s) \ll \sqrt{s}$, the description of collinear radiation by the fixed-order calculation will show unphysical enhancement or divergence. Similar to parton shower in the SM, we use the so-called dark shower to re-sum multiple radiation processes and describe this collinear radiation [64–68]. Then the result of dark shower should be merged with the fixed-order result which describes the non-collinear phase space to give a complete events distribution. Detailed discussion about dark shower and the merging method will be given in following sections.

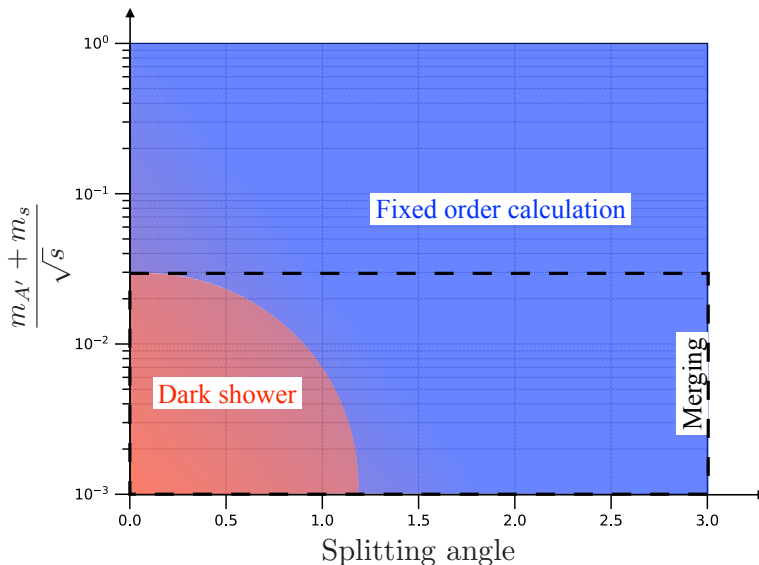


FIG. 1. Illustration for the method to deal with the dark FSR.

C Splitting functions for dark shower

The differential splitting function $d\mathcal{P}(A \rightarrow B + C)$ quantifies the probability of “finding” a parton B within a particle A. As illustrated in the left panel of Fig. 2, when the initial-state A splits collinearly into B and C, with B undergoing a hard scattering with X, since the propagator B remains approximately on-shell, the cross section can be factorized as

$$d\sigma(A + X \rightarrow C + Y) \simeq d\mathcal{P}(A \rightarrow B + C) \times d\sigma(B + X \rightarrow Y). \quad (3)$$

Analogously, if a final-state A splits collinearly (as shown in the right panel of Fig. 2), the cross section can be factorized as

$$d\sigma(X \rightarrow B + C + Y) \simeq d\sigma(X \rightarrow A + Y) \times d\mathcal{P}(A \rightarrow B + C). \quad (4)$$

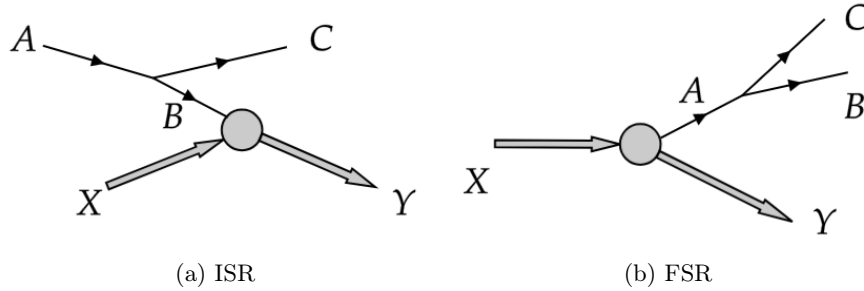


FIG. 2. The schematic diagrams of the initial-state radiation (ISR) and the final-state radiation (FSR).

$d\mathcal{P}(A \rightarrow B + C)$ is typically expressed as a function of the energy fraction of the daughter particle B relative to the mother particle A (denoted by z) and the transverse momentum of B perpendicular to the direction of A (denoted by p_T). And it can be derived by computing the invariant matrix element of the $1 \rightarrow 2$ process:

$$\frac{d\mathcal{P}}{dz dp_T^2}(A \rightarrow B + C) = \frac{1}{16\pi^2} z \bar{z} \frac{|\mathcal{M}(A \rightarrow B + C)|^2}{p_T^4}, \quad (5)$$

where $\bar{z} \equiv 1 - z$. Since $d\mathcal{P}/(dz dp_T^2)$ is always proportional to the coupling constant α' and $1/p_T^2$, the remaining factor is defined as the splitting kernel $P_{A \rightarrow B+C}(z)$,

$$\frac{d\mathcal{P}}{dz dp_T^2}(A \rightarrow B + C) = \frac{\alpha}{2\pi} P_{A \rightarrow B+C}(z) \frac{1}{p_T^2}. \quad (6)$$

Note that after spontaneous symmetry breaking, the splitting function needs to be modified to account for the acquired particle masses [62, 65],

$$\frac{d\mathcal{P}}{dz dp_T^2} \rightarrow \frac{p_T^4}{\tilde{p}_T^4} \frac{d\mathcal{P}}{dz dp_T^2}, \quad \tilde{p}_T^2 \equiv p_T^2 + \bar{z}m_B^2 + zm_C^2 - z\bar{z}m_A^2. \quad (7)$$

As for the process of the dark Higgs radiation from a dark photon $A' \rightarrow s + A'$, we provide the calculation details of splitting functions in Appendix A. In the following analysis, we focus exclusively on the leading-power results and the corresponding splitting kernels are

$$P_{A'_T \rightarrow s + A'_L}(z) = z\bar{z}, \quad (8)$$

$$P_{A'_L \rightarrow s + A'_T}(z) = \frac{2z}{\bar{z}}. \quad (9)$$

Unlike conventional parton showers, at the leading-power, the radiation of the dark Higgs alters the polarization of the dark photon, converting transverse dark photons to longitudinal ones, and vice versa. With these splitting kernels, the dark shower in our model can be realized numerically by the veto algorithm [69–71] implemented in PYTHIA8.3 [72].

III IMPACT OF THE DARK FSR

Taking the dark FSR into account, and assuming both the DP and the dark Higgs decay invisibly, the process $e^+e^- \rightarrow \gamma A' s$ presents the same signature as $e^+e^- \rightarrow \gamma A'$, i.e. mono-photon plus missing energy. Due to the emergence of the processes with dark Higgs in final-state, the search would be affected in two aspects: on the one hand, the total signal cross section increases; on the other hand, the distributions of kinematic variables - such as the squared missing mass ($M_X^2 = s - 2E_\gamma\sqrt{s}$, with E_γ being the photon energy in the center-of-mass frame) - are modified.

A Increase in the dark photon production cross section

The process $e^+e^- \rightarrow \gamma A' s$, where the final-state contains one dark Higgs, is considered as the leading-order correction to $e^+e^- \rightarrow \gamma A'$. Assuming both the dark Higgs and DP masses equal to m , and taking $\sqrt{s} = 10$ GeV, $\varepsilon = 0.01$ and $\alpha' = 0.5$, we compute the cross sections of $e^+e^- \rightarrow \gamma A'$ and $e^+e^- \rightarrow \gamma A' s$ at tree level using MADGRAPH5 [73, 74] as shown in Fig. 3. A basic cut $p_T^\gamma > 1$ GeV is applied to avoid divergence in forward region. The ratio $\sigma_{\text{ME}}(e^+e^- \rightarrow \gamma A' s)/\sigma_{\text{ME}}(e^+e^- \rightarrow \gamma A')$, which is independent of the value of ε , is also shown in the figure.

For a large m , it is reasonable to take the fixed-order matrix element (ME) calculation as the correction:

$$\sigma_{\text{FSR}} = \sigma_{\text{ME}}(e^+e^- \rightarrow \gamma A' s) \quad (\text{for large } m). \quad (10)$$

However, when $m \ll \sqrt{s}$, the physical cross section should be insensitive to the variation of m , whereas the tree-level $\sigma_{\text{ME}}(e^+e^- \rightarrow \gamma A' s)$ increases significantly as m decreases, as shown in Fig. 3. This occurs because in the $m \rightarrow 0$ limit, the collinear radiation introduces infrared (IR) divergence. In the calculation of total cross section, this IR divergence can be canceled by virtual correction [75], as promised by Kinoshita-Lee-Nauenberg theorem [76, 77]. But the physical final state distribution can not be obtained by considering virtual correction. In the following, for small m , we use the

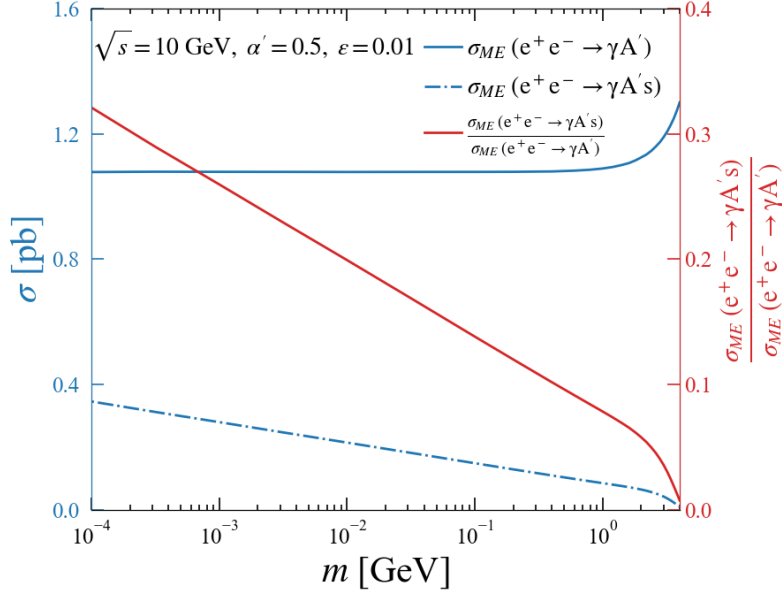


FIG. 3. The tree-level cross sections (with $p_\gamma^T > 1$ GeV) and their ratio as functions of $m = m_{A'} = m_s$. The solid and dash-dotted blue lines are the cross sections for the $e^+e^- \rightarrow \gamma A'$ and $e^+e^- \rightarrow \gamma A' s$ processes, respectively, while the red line shows their ratio.

merging method, which is the combination of dark shower and fixed-order ME, to obtain both the physical final state distribution and the cross section without divergence.

We implemented the model with FEYNRULES [78] and generated tree-level $e^+e^- \rightarrow \gamma A'$ and $e^+e^- \rightarrow \gamma A' s$ events using MADGRAPH5 [73, 74]. And the parton shower simulation of the dark FSR for the $e^+e^- \rightarrow \gamma A'$ process was performed with PYTHIA8.3 [72]. Specifically, we modified the code originally developed for the $F_v \rightarrow \gamma_v F_v$ radiation in Hidden Valley scenarios [79, 80], implemented alternating calls to the splitting kernels of $A'_T \rightarrow s A'_L$ and $A'_L \rightarrow s A'_T$ to model the timelike final-state shower of DP, adopting a transverse-momentum-ordered evolution scheme. Since only transversely polarized DPs couple to the electromagnetic current, we assume all DPs are purely transverse prior to the shower evolution at the high-energy limit.

The fraction of events radiating N_s dark Higgs bosons as a function of m is obtained from parton shower, and Fig. 4 shows the result. Even for $\alpha' = 0.5$, the probability of radiating a dark Higgs does not exceed 10%, while the probability of radiating three or more dark Higgs bosons is below 0.1%. The dark FSR probability exhibits negligible m -dependence for $m < 0.06$ GeV but decreases as m increases above this threshold.

Denoting the fraction of events with at least one dark Higgs from the dark FSR as β , the corresponding cross section is estimated as:

$$\sigma_{\text{sh}} = \frac{\beta}{1 - \beta} \sigma_{\text{ME}}(e^+e^- \rightarrow \gamma A'). \quad (11)$$

Phase space is partitioned using $\Delta R \equiv \sqrt{(\Delta\eta)^2 + (\Delta\phi)^2}$ between A' and s . For example,

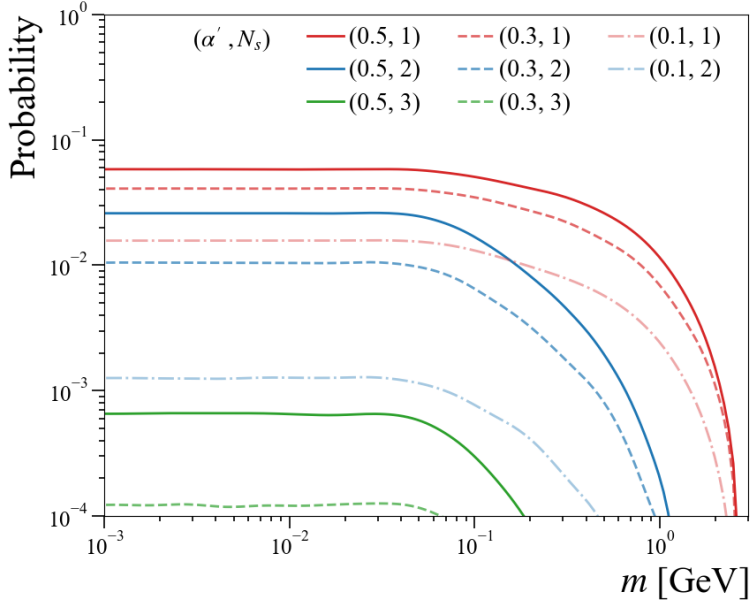


FIG. 4. The probability for a final-state DP to radiate N_s dark Higgs bosons given by the parton shower simulation. Solid, dashed and dash-dotted curves correspond to $\alpha' = 0.5, 0.3$ and 0.1 , respectively. Red, blue and green curves represent $N_s = 1, 2$ and 3 , respectively.

at $m = 0.01$ GeV and $\alpha' = 0.5$, Fig. 5 displays the ΔR distribution in which the blue line is for PYTHIA-simulated shower events and the orange line is for MadGraph-generated fixed-order events ($e^+e^- \rightarrow \gamma A's$). Using $\Delta R_{\text{cut}} = 0.5$ as the separatrix, the cross section for events with dark FSR occurring is

$$\sigma_{\text{FSR}} = P_{\text{sh}}(\Delta R < \Delta R_{\text{cut}})\sigma_{\text{sh}} + P_{\text{ME}}(\Delta R > \Delta R_{\text{cut}})\sigma_{\text{ME}}(e^+e^- \rightarrow \gamma A') \quad (\text{for small } m), \quad (12)$$

where P_{sh} and P_{ME} denote the probabilities for shower and fixed-order events to satisfy the respective ΔR criteria.

The cross section without dark FSR is

$$\sigma_{\text{no-FSR}} = \sigma_{\text{ME}}(e^+e^- \rightarrow \gamma A'). \quad (13)$$

Taking the dark FSR into account, the total signal cross section becomes

$$\sigma_{\text{sgn}} = \sigma_{\text{no-FSR}} + \sigma_{\text{FSR}}. \quad (14)$$

B Flattening of the squared missing mass distribution

Taking the square of missing mass M_X^2 as an example, we consider the effect of the dark FSR on the distributions of kinematic variables. Without dark FSR, the theoretical distribution of M_X^2

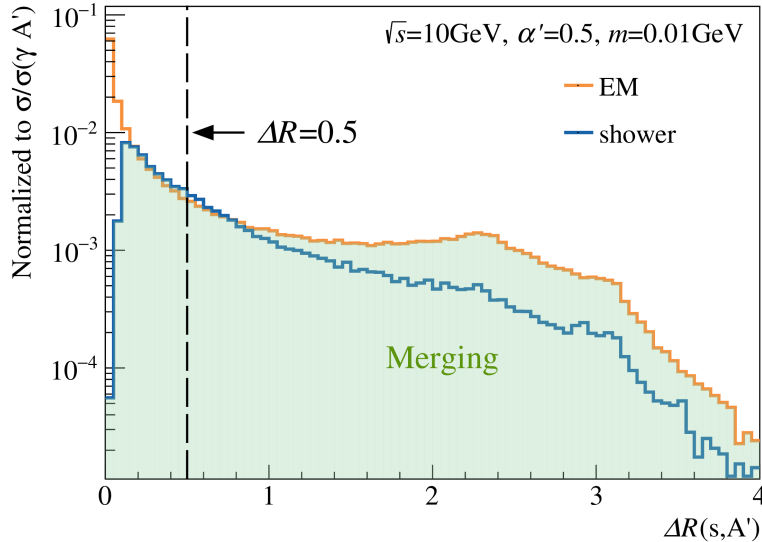


FIG. 5. The ΔR distributions and a schematic illustration of the merging procedure. The orange line represents the hard scattering process $e^+e^- \rightarrow \gamma A' s$. The blue histogram is filled with showered events of $e^+e^- \rightarrow \gamma A'$ with at least one dark Higgs boson in the final state. And both are normalized to the ratio of their respective cross sections to $\sigma_{ME}(e^+e^- \rightarrow \gamma A')$. The green shaded region represents the distribution after merging.

for the signal is a delta function centered at the DP mass $m_{A'}$,

$$f_{\text{no-FSR}}^{\text{th}}(M_X^2) = \delta(M_X^2 - m_{A'}^2). \quad (15)$$

When dark FSR is included, the fraction of signal events in which the DP does not radiate a dark Higgs is given by

$$\lambda = \frac{\sigma_{\text{no-FSR}}}{\sigma_{\text{no-FSR}} + \sigma_{\text{FSR}}}. \quad (16)$$

The M_X^2 distribution for this part of events is still given by $f_{\text{no-FSR}}^{\text{th}}(M_X^2)$. But for the remaining fraction $(1 - \lambda)$ of events containing at least one dark Higgs, the value of M_X^2 , which represents the square of invariant mass of all invisible particles, would increase due to the dark FSR, and its distribution should be described by another function $f_{\text{FSR}}^{\text{th}}(M_X^2)$.

The function $f_{\text{FSR}}^{\text{th}}(M_X^2)$ can be approximated by the following method: First, generate events via Monte Carlo (MC) simulation and fill into the histogram of M_X^2 . Then perform a linear interpolation and normalization on this histogram. Note that in the low-mass region, the merged MC events are used.

The theoretical M_X^2 distribution for the signal considering dark FSR is then the weighted sum

$$f^{\text{th}}(M_X^2) = \lambda f_{\text{no-FSR}}^{\text{th}}(M_X^2) + (1 - \lambda) f_{\text{FSR}}^{\text{th}}(M_X^2). \quad (17)$$

The experimentally observed signal distribution $f_{\text{sgn}}(M_X^2)$ results from the convolution of this theoretical distribution $f^{\text{th}}(M_X^2)$ with the detector resolution function $f^{\text{re}}(M_X^2)$,

$$\begin{aligned} f_{\text{sgn}}(M_X^2) &= f^{\text{th}}(M_X^2) \otimes f^{\text{re}}(M_X^2) \\ &= \lambda [f_{\text{no-FSR}}^{\text{th}}(M_X^2) \otimes f^{\text{re}}(M_X^2)] + (1 - \lambda) [f_{\text{FSR}}^{\text{th}}(M_X^2) \otimes f^{\text{re}}(M_X^2)]. \end{aligned} \quad (18)$$

The convolution for the non-FSR component simplifies to a shift of the resolution function,

$$\begin{aligned} f_{\text{no-FSR}}(M_X^2) &= f_{\text{no-FSR}}^{\text{th}}(M_X^2) \otimes f^{\text{re}}(M_X^2) \\ &= \delta(M_X^2 - m_{A'}^2) \otimes f^{\text{re}}(M_X^2) = f^{\text{re}}(M_X^2 - m_{A'}^2). \end{aligned} \quad (19)$$

Therefore, the signal distribution is

$$f_{\text{sgn}}(M_X^2) = \lambda f^{\text{re}}(M_X^2 - m_{A'}^2) + (1 - \lambda) [f_{\text{FSR}}^{\text{th}}(M_X^2) \otimes f^{\text{re}}(M_X^2)]. \quad (20)$$

So the distribution of M_X^2 for the signal becomes flattened compared to $f_{\text{no-FSR}}(M_X^2)$.

IV RECASTING BABAR ANALYSIS WITH DARK FSR EFFECTS

For the $e^+e^- \rightarrow \gamma A'$ channel with $A' \rightarrow$ invisible, the BaBar collaboration has analyzed data collected at the PEP-II B-Factory near the $\Upsilon(2S)$, $\Upsilon(3S)$, and $\Upsilon(4S)$ resonance peaks ($\sqrt{s} \sim 10$ GeV), with an integrated luminosity of 53 fb^{-1} [34]. They derived the exclusion limit on the mixing parameter ε via a maximum likelihood fit to the distribution of M_X^2 . In this section, we quantify the specific impact of the dark FSR on BaBar's exclusion limit under the assumption $\alpha' = 0.5$ and for m in the range $[0.001, 2]$ GeV.

A Decompose the impact

Let N_0 denotes the original signal count upper limit without dark FSR, corresponding to a mixing parameter upper limit ε_0 . With dark FSR considered, they become N' and ε' , respectively. Since the signal count is proportional to the cross section, and the cross section scales quadratically with the mixing parameter,

$$N_0 \propto \sigma_{\text{no-FSR}}(\varepsilon = \varepsilon_0) = \varepsilon_0^2 \sigma_{\text{no-FSR}}(\varepsilon = 1), \quad (21)$$

$$N' \propto \sigma_{\text{sgn}}(\varepsilon = \varepsilon') = \varepsilon'^2 \sigma_{\text{sgn}}(\varepsilon = 1), \quad (22)$$

we can separate the impact of the dark FSR into two parts

$$\frac{\varepsilon'^2}{\varepsilon_0^2} = \frac{N'}{N_0} \frac{\sigma_{\text{no-FSR}}(\varepsilon = 1)}{\sigma_{\text{sgn}}(\varepsilon = 1)} = S_{\text{fit}} \cdot S_{\text{cxs}}. \quad (23)$$

Here, $S_{\text{fit}} \equiv N'/N_0$ represents the correction factor due to the altered signal shape affecting the fit, while $S_{\text{cxs}} \equiv \sigma_{\text{no-FSR}}/\sigma_{\text{sgn}}$ is the correction factor from the cross section increase.

B Effect of signal distribution

Taking $m = 0.01$ GeV as an example, the variation of M_X^2 distribution caused by the dark FSR is simulated. The $f_{\text{FSR}}^{\text{th}}(M_X^2)$ is obtained via linear interpolation of the histogram from simulated events as described in Sec. III B. The detector response function $f^{\text{re}}(M_X^2)$ is modeled by a Crystal Ball function with resolution $\sigma(M_X^2) = 1.5$ GeV², and other parameters are determined by fitting the signal peak in Fig.3 of Ref. [34]. To calculate $f_{\text{FSR}}(M_X^2) = f_{\text{FSR}}^{\text{th}}(M_X^2) \otimes f^{\text{re}}(M_X^2)$, we perform a numerical convolution with Fourier transforms in the interval $[-10, 50]$ GeV² using ROOFIT [81, 82], with a sampling frequency of 10,000. The $f_{\text{FSR}}(M_X^2)$ represents the distribution for these events in which the dark FSR does occur and is shown as the blue dashed line in Fig. 6. According to Eq. 19 and Eq. 20, we get the distributions for signal considering dark FSR or not as indicated by the red line and black dotted line respectively in Fig. 6.

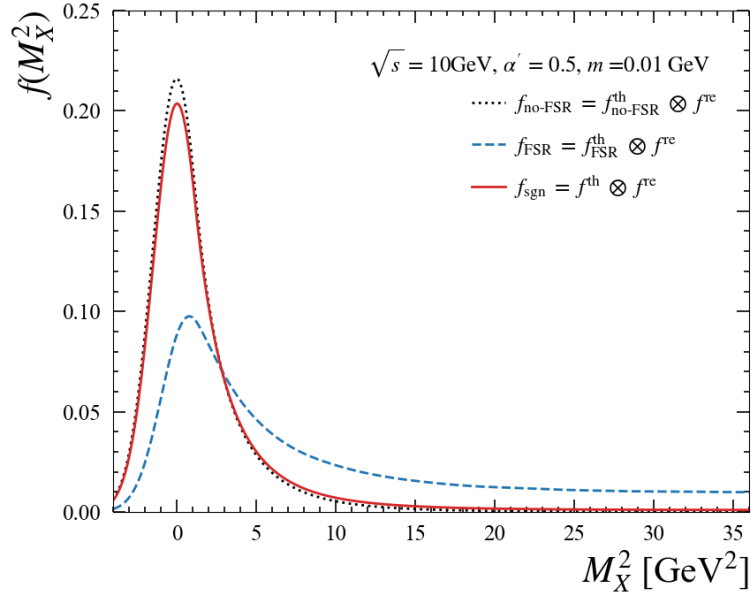


FIG. 6. Probability density functions (PDFs) of M_X^2 for signal. The black dotted curve represents the no-FSR scenario, the red solid curve includes dark FSR effects, and the blue dashed curve corresponds to the component that radiated dark Higgs.

Notably, as the blue line shows, the radiation of dark Higgs bosons shifts the missing mass squared M_X^2 to higher values, flattening the peak, shifting it rightward, and generating a pronounced tail on the high- M_X^2 side. However, since only a small fraction of events radiate (no more than 10% for $\alpha' = 0.5$), the $f_{\text{sgn}}(M_X^2)$ closely resembles the no-FSR distribution, differing only by a slight reduction in peak height and a moderate broadening of the tail on the right side.

To study the impact of changes in signal distribution on experimental results, we perform a simplified recast of the BaBar analysis. There are 6 signal regions for the low-mass situation, and for simplicity, we only focus on the region near the $\Upsilon(3S)$ resonance satisfying the \mathcal{R}'_L selection

criteria, which contains 129 events, more than the sum of the other five regions. The binned data and the background-only fit are provided in the supplementary material of Ref. [34](see Fig. 7). We decompose the background-only fit into a Crystal Ball function describing the peaking background from $e^+e^- \rightarrow \gamma\gamma$ and a second-order polynomial which primarily comes from Bhabha scattering $e^+e^- \rightarrow \gamma e^+e^-$.

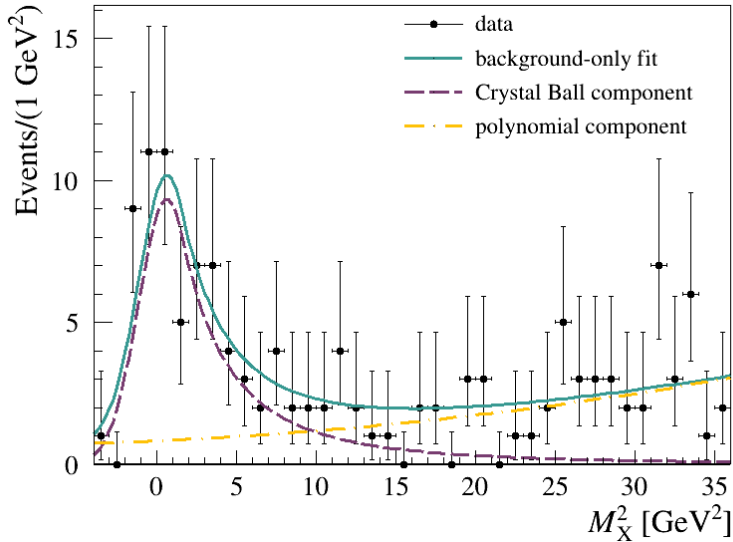


FIG. 7. The distribution of M_X^2 in the low- M_X^2 region with data samples collected near $\Upsilon(3S)$ resonance and selected with \mathcal{R}'_L . Both the histogram and the curve of the background-only fit are taken from the supplementary material of Ref. [34].

The signal shape influences the confidence intervals by affecting the likelihood function under the signal-plus-background (S+B) hypothesis. When constructing the profile-likelihood ratio test statistic, background event counts (total and peaking) are treated as nuisance parameters, and the integral values of the corresponding curves in Fig. 7 are set as the global observables. Performing hypothesis test inversion using ROOSTATS [83, 84], we obtain the 90% confidence level (C.L.) upper limits (based on the CLs method) on the signal yield: $N_0 = 18.1$ (without dark FSR) and $N' = 18.5$ (with dark FSR). The slight increase in the upper limit arises because incorporating dark FSR leads to a broader signal shape $f_{sgn}(M_X^2)$, marginally degrading the experimental sensitivity. Repeating this for different m values yields $S_{\text{fit}} \equiv N'/N_0$, which is always in the range of 1.03 to 1.04.

C Effect of cross section

To get the limit on the mixing parameter ε , the cross section satisfying specific selection criteria is requisite. Consistent with Ref. [34], the following cuts are taken: $E_\gamma > 3$ GeV, $|\cos\theta_\gamma| < 0.6$, and $-4 < M_X^2 < 36$ GeV², where E_γ and $\cos\theta_\gamma$ represent energy and polar angle of photon in the

center-of-mass frame. Note that the cut efficiency is also influenced by the PDF of M_X^2 for signal. For the cross section σ_{FSR} corresponding to the signal component where dark Higgs bosons are radiated, we utilize the merging result for $m < 0.05$ GeV (as in Eq. 12) and ME result for $m > 0.25$ GeV (as in Eq. 10), with a smooth interpolation applied in the intermediate mass region. According to Eq. 14, the resulting cross section assuming $\varepsilon = 0.01$ is gotten and presented in Fig. 8.

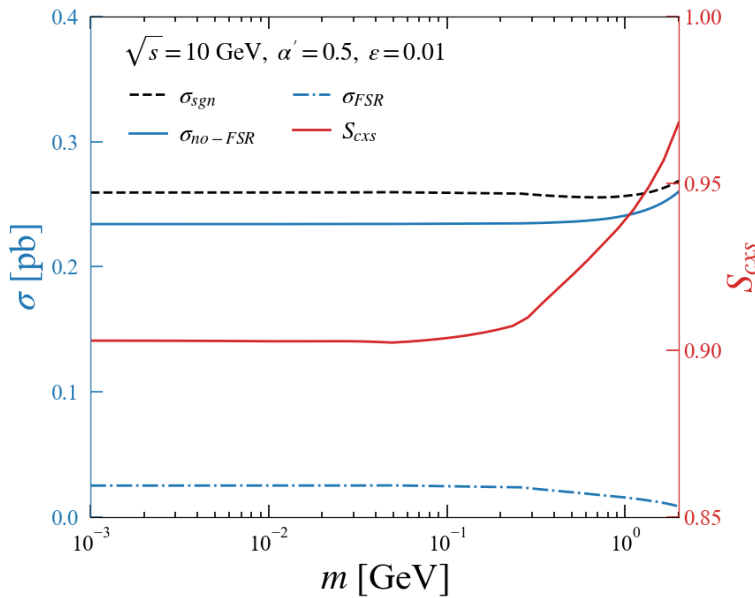


FIG. 8. The signal cross sections as functions of $m = m_{A'} = m_s$. The black dashed curve represents the cross section incorporating dark FSR. The solid and dash-dotted blue lines are for the components without or with dark Higgs bosons in final state, respectively. The red line represents the correction factor $S_{\text{cxs}} \equiv \sigma_{\text{no-FSR}}/\sigma_{\text{sgn}}$ introduced to ε^2 due to the cross section variation.

For $m < 0.1$ GeV, the cross section is not sensitive to the mass, and the correction factor S_{cxs} introduced by the cross section variation is about 0.90. For $m > 0.1$ GeV, as the mass increases, the cross section for the two-body final state increases since the electron propagator approaching the on-shell state. Conversely, the FSR cross section reduces due to phase space suppression. Note that this decrease depends on the assumption $m = m_{A'} = m_s$.

D New limit on the mixing parameter

Following Eq. 23, the exclusion limit ε' incorporating dark FSR effect is derived and shown as the red dashed curve in Fig. 9. This limit lies slightly below the limit ε_0 obtained without dark FSR by BaBar. For $m < 0.2$ GeV, $\varepsilon'/\varepsilon_0 \approx 0.97$. Then as m increases, $\varepsilon'/\varepsilon_0$ rises gradually. At $m = 2$ GeV, $\varepsilon'/\varepsilon_0 \approx 1$.

The relative uncertainty of the upper limit at 90% C.L. of ε introduced by the dark Higgs mechanism is estimated as $|\varepsilon_0 - \varepsilon'|/\varepsilon_0$. Its maximum value is about 3.4%, which is comparable

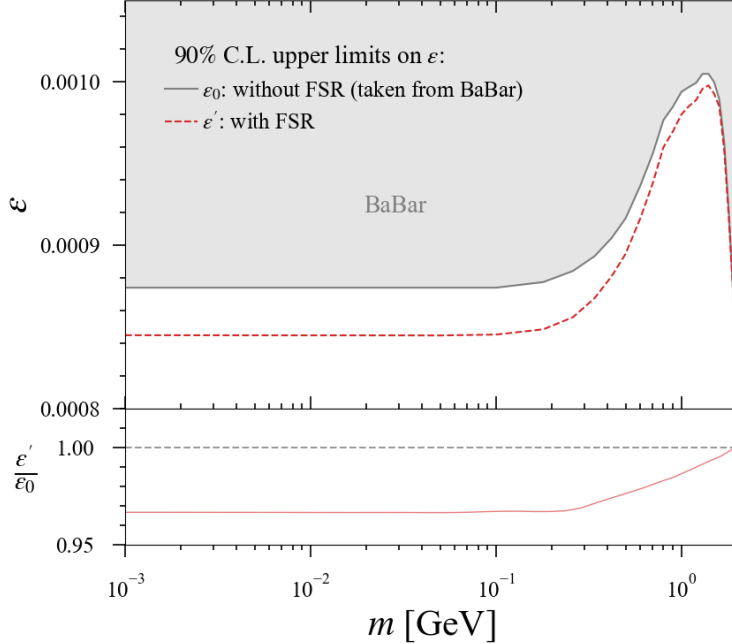


FIG. 9. Upper limits on the mixing parameter ε at 90% C.L., comparing scenarios with and without dark FSR. The gray curve corresponds to the profile-likelihood limit from BaBar[34]. The red dashed curve shows the exclusion limit incorporating dark FSR effects from the dark Higgs mechanism, under the assumption $\alpha' = 0.5$ and $m = m_{A'} = m_s$. The red line in the lower panel gives the ratio of the new limit to the BaBar limit.

to the total multiplicative error on the signal cross section (5%) given in the original analysis by BaBar, but remains negligible compared to the statistical uncertainty.

V CONCLUSION

In this work, we investigated how the emergence of the dark Higgs particle would affect the collider detection of dark photons. A dark sector model with a spontaneously broken $U(1)'$ is given. In this model, it is possible for a high energy dark photon to emit a dark Higgs via dark FSR $A' \rightarrow A's$.

For the $e^+e^- \rightarrow \gamma A'$ channel searching for invisible DPs, we analyzed the impact of the dark FSR from two aspects: The increase of cross section at a fixed ε would strengthen the exclusion limit (lowering the upper bound on ε); The broadening of the signal's distribution reduces detection sensitivity, thereby relaxing the constraint.

Through a recast of the BaBar experiment, we derived a new exclusion limit on the kinetic mixing parameter ε . Since the cross-section enhancement effect dominates, the new limit is moderately stronger than the original result. In the region where both the DP and dark Higgs masses are below

0.2 GeV, the upper limit is lowered by approximately 3%.

ACKNOWLEDGEMENTS

We appreciate helpful discussions with Alessandra Filippi, Haitao Li, Yang Ma, Lianyou Shan, Brian Shuve, Lei Wu, Yongchao Zhang and Yu Zhang. This work is supported by the National Natural Science Foundation of China under Grant Nos. 12335005, 12105248, 12105118 and 11947118, by the Peng-Huan-Wu Theoretical Physics Innovation Center funded by the National Natural Science Foundation of China (Grant No.12447101) and by the Research Fund for PI from Henan Normal University under Grant No. 5101029470335.

A DERIVATION OF SPLITTING FUNCTIONS

In this appendix, we give some details in the calculation of the splitting functions for the process $A' \rightarrow sA'$, includes Feynman rules and the setting of kinematics.

1 Feynman rules

The Lagrangian is given in Eq. 1. Adopting the Goldstone Equivalence Gauge following Ref. [62], the contribution of the Goldstone component in the longitudinally polarized dark photon can be disentangled, with the gauge-fixing term specified as

$$\mathcal{L}_{fix} = -\frac{1}{2\xi}(n \cdot A)(n^* \cdot A), (\xi \rightarrow 0), \quad (\text{A1})$$

in which

$$n^\mu(k) \equiv (1, -\hat{\mathbf{k}}). \quad (\text{A2})$$

The masses of s and A' are

$$m_s = \sqrt{\frac{\lambda}{2}}v, \quad m_{A'} = g'v. \quad (\text{A3})$$

The coupling terms of $A'A's$, aas and $A'as$ are $g'^2vA'_\mu A'^\mu s$, $-\frac{1}{4}\lambda va^2s$ and $g'(a\partial_\mu s - s\partial_\mu a)A'^\mu$ respectively, from which the following Feynman rules are derived:

The figure shows three Feynman diagrams representing the splitting functions for the process $A' \rightarrow sA'$. Each diagram is equated to a mathematical expression. The first diagram shows an incoming A' line (wavy) splitting into an outgoing s line (dashed) and an outgoing A' line (wavy), with the value $2ig'^2v$. The second diagram shows an incoming a line (dashed) splitting into an outgoing s line (dashed) and an outgoing a line (dashed), with the value $-\frac{i}{2}\lambda v$. The third diagram shows an incoming A'^μ line (wavy) splitting into an outgoing s line (dashed) and an outgoing a line (dashed), with momenta p_s and p_a indicated by arrows, and the value $g'(p_a^\mu - p_s^\mu)$.

$$A' \rightsquigarrow \begin{matrix} s \\ A' \end{matrix} = 2ig'^2v, \quad a \rightsquigarrow \begin{matrix} s \\ a \end{matrix} = -\frac{i}{2}\lambda v, \quad A'^\mu \rightsquigarrow \begin{matrix} p_s \nearrow s \\ p_a \searrow a \end{matrix} = g'(p_a^\mu - p_s^\mu) \quad (\text{A4})$$

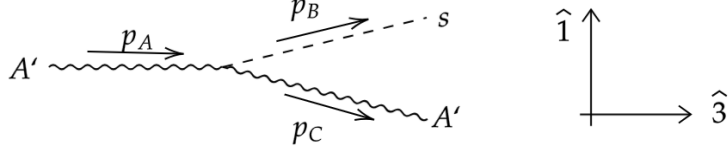


FIG. 10. The setting of kinematic variables.

The a - A' mixing term $-g'vA'^\mu\partial_\mu a = -m_{A'}A'^\mu\partial_\mu a$ leads to

$$A'^\mu \text{ wavy} \xrightarrow{p_a} a = m_{A'} p_a^\mu. \quad (\text{A5})$$

For the longitudinal A' , which contains both the Goldstone component a and the gauge component A'_n , the relative phase between them must be considered. In the light of the Ward identity, a phase factor $-i$ is assigned to the initial-state a , while a phase factor i is introduced for the final-state a .

2 Kinematics

In the high-energy limit, we establish the coordinate system as illustrated in Fig. 10 and define kinematic variables accurate up to $\mathcal{O}(p_T)$,

$$\begin{aligned} p_A &= (p, 0, 0, p), \\ p_B &= (zp, p_T, 0, zp), \\ p_C &= ((1-z)p, -p_T, 0, (1-z)p). \end{aligned} \quad (\text{A6})$$

The transversely polarized vectors are

$$\begin{aligned} \epsilon_{A+}^\mu &= \frac{1}{\sqrt{2}}(0, 1, i, 0), \epsilon_{A-}^\mu = \frac{1}{\sqrt{2}}(0, 1, -i, 0), \\ \epsilon_{C+}^\mu &= \frac{1}{\sqrt{2}}\left(0, 1, i, \frac{p_T}{(1-z)p}\right), \epsilon_{C-}^\mu = \frac{1}{\sqrt{2}}\left(0, 1, -i, \frac{p_T}{(1-z)p}\right). \end{aligned} \quad (\text{A7})$$

And in the Goldstone Equivalence Gauge, the longitudinally polarized vector is

$$\epsilon_L^\mu = \frac{k^\mu}{m_{A'}} - \frac{m_{A'}}{n \cdot k} n^\mu. \quad (\text{A8})$$

Here, the term $\frac{k^\mu}{m_{A'}}$ corresponds to the Goldstone component, while the other term is defined as $\epsilon_n^\mu \equiv -\frac{m_{A'}}{n \cdot k} n^\mu$ and can be specifically written as

$$\epsilon_{An}^\mu = \frac{m_{A'}}{2p}(-1, 0, 0, 1), \epsilon_{Cn}^\mu = \frac{m_{A'}}{2(1-z)p}\left(-1, -\frac{p_T}{(1-z)p}, 0, 1\right). \quad (\text{A9})$$

3 Results of the calculation

Substituting the Feynman rules and kinematic variables into Eq. 5, we compute the splitting functions. The leading-power contribution ($\propto \frac{p_T^2}{\tilde{p}_T^4}$) yields

$$\frac{d\mathcal{P}}{dzdk_T^2}(A'_T \rightarrow s + A'_L) = \frac{\alpha'}{2\pi} z\bar{z} \frac{p_T^2}{\tilde{p}_T^4}, \quad (\text{A10})$$

$$\frac{d\mathcal{P}}{dzdk_T^2}(A'_L \rightarrow s + A'_T) = \frac{\alpha'}{2\pi} \frac{2z}{\bar{z}} \frac{p_T^2}{\tilde{p}_T^4}. \quad (\text{A11})$$

Note that the radiation of the dark Higgs alters the polarization of the dark photon. Furthermore, in the high-energy limit, the amplitudes $\mathcal{M}(A'_T \rightarrow s + A'_n)$ and $\mathcal{M}(A'_n \rightarrow s + A'_T)$, which involve the gauge longitudinal component and scale as $\frac{m_{A'}^2}{p^2}$, are suppressed. Consequently, the leading-power contribution arises solely from the Goldstone component in the longitudinally polarized dark photon, consistent with the Goldstone equivalence theorem.

Splitting processes preserving the polarization of the dark photon contribute at next-to-leading power ($\propto \frac{m_{A'}^2}{\tilde{p}_T^4}$):

$$\frac{d\mathcal{P}}{dzdk_T^2}(A'_T \rightarrow s + A'_T) = \frac{\alpha'}{2\pi} 2z\bar{z} \frac{m_{A'}^2}{\tilde{p}_T^4}, \quad (\text{A12})$$

$$\frac{d\mathcal{P}}{dzdk_T^2}(A'_L \rightarrow s + A'_L) = \frac{\alpha'}{2\pi} \frac{z\bar{z}}{2} \left(\frac{m_s^2}{m_{A'}^2} + \frac{2(1-z\bar{z})}{\bar{z}} \right)^2 \frac{m_{A'}^2}{\tilde{p}_T^4}. \quad (\text{A13})$$

-
- [1] D. Abercrombie *et al.*, *Phys. Dark Univ.* **27**, 100371 (2020), arXiv:1507.00966 [hep-ex].
 - [2] A. Tan *et al.* (PandaX-II), *Phys. Rev. Lett.* **117**, 121303 (2016), arXiv:1607.07400 [hep-ex].
 - [3] D. S. Akerib *et al.* (LUX), *Phys. Rev. Lett.* **118**, 021303 (2017), arXiv:1608.07648 [astro-ph.CO].
 - [4] M. Aaboud *et al.* (ATLAS), *Eur. Phys. J. C* **77**, 393 (2017), arXiv:1704.03848 [hep-ex].
 - [5] G. Aad *et al.* (ATLAS), *Phys. Rev. Lett.* **112**, 041802 (2014), arXiv:1309.4017 [hep-ex].
 - [6] V. Khachatryan *et al.* (CMS), *JHEP* **12**, 088 (2016), arXiv:1603.08914 [hep-ex].
 - [7] M. Aaboud *et al.* (ATLAS), *Phys. Rev. Lett.* **119**, 181804 (2017), arXiv:1707.01302 [hep-ex].
 - [8] N. Arkani-Hamed, D. P. Finkbeiner, T. R. Slatyer, and N. Weiner, *Phys. Rev. D* **79**, 015014 (2009), arXiv:0810.0713 [hep-ph].
 - [9] M. Pospelov and A. Ritz, *Phys. Lett. B* **671**, 391 (2009), arXiv:0810.1502 [hep-ph].
 - [10] D. S. M. Alves, S. R. Behbahani, P. Schuster, and J. G. Wacker, *Phys. Lett. B* **692**, 323 (2010), arXiv:0903.3945 [hep-ph].
 - [11] J. Hisano, S. Matsumoto, and M. M. Nojiri, *Phys. Rev. Lett.* **92**, 031303 (2004), arXiv:hep-ph/0307216.
 - [12] J. March-Russell, S. M. West, D. Cumberbatch, and D. Hooper, *JHEP* **07**, 058 (2008), arXiv:0801.3440 [hep-ph].
 - [13] N. Arkani-Hamed and N. Weiner, *JHEP* **12**, 104 (2008), arXiv:0810.0714 [hep-ph].
 - [14] M. Cirelli, M. Kadastik, M. Raidal, and A. Strumia, *Nucl. Phys. B* **813**, 1 (2009), [Addendum: *Nucl.Phys.B* 873, 530–533 (2013)], arXiv:0809.2409 [hep-ph].

- [15] M. Pospelov, A. Ritz, and M. B. Voloshin, *Phys. Lett. B* **662**, 53 (2008), arXiv:0711.4866 [hep-ph].
- [16] I. Cholis, G. Dobler, D. P. Finkbeiner, L. Goodenough, and N. Weiner, *Phys. Rev. D* **80**, 123518 (2009), arXiv:0811.3641 [astro-ph].
- [17] I. Cholis, D. P. Finkbeiner, L. Goodenough, and N. Weiner, *JCAP* **12**, 007 (2009), arXiv:0810.5344 [astro-ph].
- [18] T. G. Rizzo, *Phys. Rev. D* **110**, 075037 (2024), arXiv:2408.01296 [hep-ph].
- [19] C. Ahdida *et al.* (SHiP), *Eur. Phys. J. C* **82**, 486 (2022), arXiv:2112.01487 [physics.ins-det].
- [20] B. Aubert *et al.* (BaBar), *Nucl. Instrum. Meth. A* **479**, 1 (2002), arXiv:hep-ex/0105044.
- [21] A. Abashian *et al.* (Belle), *Nucl. Instrum. Meth. A* **479**, 117 (2002).
- [22] M. Ablikim *et al.* (BESIII), *Nucl. Instrum. Meth. A* **614**, 345 (2010), arXiv:0911.4960 [physics.ins-det].
- [23] M. Adinolfi *et al.*, *Nucl. Instrum. Meth. A* **488**, 51 (2002).
- [24] S. Andreas *et al.*, (2013), arXiv:1312.3309 [hep-ex].
- [25] D. Banerjee *et al.* (NA64), *Phys. Rev. Lett.* **118**, 011802 (2017), arXiv:1610.02988 [hep-ex].
- [26] S. N. Gninenko, *Phys. Rev. D* **89**, 075008 (2014), arXiv:1308.6521 [hep-ph].
- [27] D. Banerjee *et al.* (NA64), *Phys. Rev. D* **97**, 072002 (2018), arXiv:1710.00971 [hep-ex].
- [28] J. Chen *et al.* (DarkSHINE), *Sci. China Phys. Mech. Astron.* **66**, 211062 (2023).
- [29] J. L. Feng, I. Galon, F. Kling, and S. Trojanowski, *Phys. Rev. D* **97**, 035001 (2018), arXiv:1708.09389 [hep-ph].
- [30] H. Abreu *et al.* (FASER), *JINST* **19**, P05066 (2024), arXiv:2207.11427 [physics.ins-det].
- [31] A. A. Alves, Jr. *et al.* (LHCb), *JINST* **3**, S08005 (2008).
- [32] D. Banerjee *et al.*, *Phys. Rev. Lett.* **123**, 121801 (2019), arXiv:1906.00176 [hep-ex].
- [33] Y. Zhang, W.-T. Zhang, M. Song, X.-A. Pan, Z.-M. Niu, and G. Li, *Phys. Rev. D* **100**, 115016 (2019), arXiv:1907.07046 [hep-ph].
- [34] J. P. Lees *et al.* (BaBar), *Phys. Rev. Lett.* **119**, 131804 (2017), arXiv:1702.03327 [hep-ex].
- [35] M. Ablikim *et al.* (BESIII), *Phys. Lett. B* **774**, 252 (2017), arXiv:1705.04265 [hep-ex].
- [36] P. Ilten, J. Thaler, M. Williams, and W. Xue, *Phys. Rev. D* **92**, 115017 (2015), arXiv:1509.06765 [hep-ph].
- [37] D. Babusci *et al.* (KLOE-2), *Phys. Lett. B* **720**, 111 (2013), arXiv:1210.3927 [hep-ex].
- [38] A. Anastasi *et al.* (KLOE-2), *Phys. Lett. B* **757**, 356 (2016), arXiv:1603.06086 [hep-ex].
- [39] P. Ilten, Y. Soreq, J. Thaler, M. Williams, and W. Xue, *Phys. Rev. Lett.* **116**, 251803 (2016), arXiv:1603.08926 [hep-ph].
- [40] H. Merkel *et al.*, *Phys. Rev. Lett.* **112**, 221802 (2014), arXiv:1404.5502 [hep-ex].
- [41] J. P. Lees *et al.* (BaBar), *Phys. Rev. Lett.* **113**, 201801 (2014), arXiv:1406.2980 [hep-ex].
- [42] F. Archilli *et al.* (KLOE-2), *Phys. Lett. B* **706**, 251 (2012), arXiv:1110.0411 [hep-ex].
- [43] R. Aaij *et al.* (LHCb), *Phys. Rev. Lett.* **124**, 041801 (2020), arXiv:1910.06926 [hep-ex].
- [44] D. Babusci *et al.* (KLOE-2), *Phys. Lett. B* **736**, 459 (2014), arXiv:1404.7772 [hep-ex].
- [45] J. R. Batley *et al.* (NA48/2), *Phys. Lett. B* **746**, 178 (2015), arXiv:1504.00607 [hep-ex].
- [46] W. Altmannshofer *et al.* (Belle-II), *PTEP* **2019**, 123C01 (2019), [Erratum: PTEP 2020, 029201 (2020)], arXiv:1808.10567 [hep-ex].
- [47] B. W. Lee, C. Quigg, and H. B. Thacker, *Phys. Rev. Lett.* **38**, 883 (1977).
- [48] B. W. Lee, C. Quigg, and H. B. Thacker, *Phys. Rev. D* **16**, 1519 (1977).
- [49] S. Li, J. M. Yang, M. Zhang, and R. Zhu, *Phys. Rev. D* **111**, 035005 (2025), arXiv:2405.18226 [hep-ph].
- [50] Z. Chen, K. Ye, and M. Zhang, *Phys. Rev. D* **107**, 095027 (2023), arXiv:2303.11820 [hep-ph].
- [51] I. Baldes and K. Petraki, *JCAP* **09**, 028 (2017), arXiv:1703.00478 [hep-ph].

- [52] M. L. Graesser, I. M. Shoemaker, and L. Vecchi, *JHEP* **10**, 110 (2011), [arXiv:1103.2771 \[hep-ph\]](#).
- [53] M. Ibe, A. Kamada, S. Kobayashi, T. Kuwahara, and W. Nakano, *Phys. Rev. D* **100**, 075022 (2019), [arXiv:1907.03404 \[hep-ph\]](#).
- [54] B. Batell, M. Pospelov, and A. Ritz, *Phys. Rev. D* **79**, 115008 (2009), [arXiv:0903.0363 \[hep-ph\]](#).
- [55] K. Cheung, Y. Kim, Y. Kwon, C. J. Ouseph, A. Soffer, and Z. S. Wang, *JHEP* **05**, 094 (2024), [arXiv:2401.03168 \[hep-ph\]](#).
- [56] F. Abudinén *et al.* (Belle-II), *Phys. Rev. Lett.* **130**, 071804 (2023), [arXiv:2207.00509 \[hep-ex\]](#).
- [57] A. Anastasi *et al.* (KLOE-2), *Phys. Lett. B* **747**, 365 (2015), [arXiv:1501.06795 \[hep-ex\]](#).
- [58] J. P. Lees *et al.* (BaBar), *Phys. Rev. Lett.* **108**, 211801 (2012), [arXiv:1202.1313 \[hep-ex\]](#).
- [59] I. Jaegle (Belle), *Phys. Rev. Lett.* **114**, 211801 (2015), [arXiv:1502.00084 \[hep-ex\]](#).
- [60] M. Buschmann, J. Kopp, J. Liu, and P. A. N. Machado, *JHEP* **07**, 045 (2015), [arXiv:1505.07459 \[hep-ph\]](#).
- [61] M. Kim, H.-S. Lee, M. Park, and M. Zhang, *Phys. Rev. D* **98**, 055027 (2018), [arXiv:1612.02850 \[hep-ph\]](#).
- [62] J. Chen, P. Ko, H.-N. Li, J. Li, and H. Yokoya, *JHEP* **01**, 141 (2019), [arXiv:1807.00530 \[hep-ph\]](#).
- [63] S. Chigusa and M. Yamazaki, *Phys. Lett. B* **834**, 137466 (2022), [arXiv:2204.12500 \[hep-ph\]](#).
- [64] M. Bengtsson and T. Sjostrand, *Nucl. Phys. B* **289**, 810 (1987).
- [65] J. Chen, T. Han, and B. Tweedie, *JHEP* **11**, 093 (2017), [arXiv:1611.00788 \[hep-ph\]](#).
- [66] J. C. Collins, D. E. Soper, and G. F. Sterman, *Nucl. Phys. B* **250**, 199 (1985).
- [67] J. C. Collins, D. E. Soper, and G. F. Sterman, *Adv. Ser. Direct. High Energy Phys.* **5**, 1 (1989), [arXiv:hep-ph/0409313](#).
- [68] V. V. Sudakov, *Sov. Phys. JETP* **3**, 65 (1956).
- [69] S. Hoeche, S. Schumann, and F. Siegert, *Phys. Rev. D* **81**, 034026 (2010), [arXiv:0912.3501 \[hep-ph\]](#).
- [70] L. Lönnblad, *Eur. Phys. J. C* **73**, 2350 (2013), [arXiv:1211.7204 \[hep-ph\]](#).
- [71] S. Mrenna and P. Skands, *Phys. Rev. D* **94**, 074005 (2016), [arXiv:1605.08352 \[hep-ph\]](#).
- [72] C. Bierlich *et al.*, (2022), [10.21468/SciPostPhysCodeb.8](#), [arXiv:2203.11601 \[hep-ph\]](#).
- [73] J. Alwall, R. Frederix, S. Frixione, V. Hirschi, F. Maltoni, O. Mattelaer, H. S. Shao, T. Stelzer, P. Torrielli, and M. Zaro, *JHEP* **07**, 079 (2014), [arXiv:1405.0301 \[hep-ph\]](#).
- [74] R. Frederix, S. Frixione, V. Hirschi, D. Pagani, H. S. Shao, and M. Zaro, *JHEP* **07**, 185 (2018), [Erratum: *JHEP* 11, 085 (2021)], [arXiv:1804.10017 \[hep-ph\]](#).
- [75] P. S. B. Dev, D. Kim, D. Sathyan, K. Sinha, and Y. Zhang, (2024), [arXiv:2407.12738 \[hep-ph\]](#).
- [76] T. Kinoshita, *J. Math. Phys.* **3**, 650 (1962).
- [77] T. D. Lee and M. Nauenberg, *Phys. Rev.* **133**, B1549 (1964).
- [78] A. Alloul, N. D. Christensen, C. Degrande, C. Duhr, and B. Fuks, *Comput. Phys. Commun.* **185**, 2250 (2014), [arXiv:1310.1921 \[hep-ph\]](#).
- [79] L. Carloni and T. Sjostrand, *JHEP* **09**, 105 (2010), [arXiv:1006.2911 \[hep-ph\]](#).
- [80] L. Carloni, J. Rathsman, and T. Sjostrand, *JHEP* **04**, 091 (2011), [arXiv:1102.3795 \[hep-ph\]](#).
- [81] W. Verkerke and D. P. Kirkby, eConf **C0303241**, MOLT007 (2003), [arXiv:physics/0306116](#).
- [82] M. Frigo and S. G. Johnson, *Proceedings of the IEEE* **93**, 216 (2005), special issue on “Program Generation, Optimization, and Platform Adaptation”.
- [83] L. Moneta, K. Belasco, K. S. Cranmer, S. Kreiss, A. Lazzaro, D. Piparo, G. Schott, W. Verkerke, and M. Wolf, *PoS ACAT2010*, 057 (2010), [arXiv:1009.1003 \[physics.data-an\]](#).
- [84] G. Cowan, K. Cranmer, E. Gross, and O. Vitells, *Eur. Phys. J. C* **71**, 1554 (2011), [Erratum: *Eur.Phys.J.C* 73, 2501 (2013)], [arXiv:1007.1727 \[physics.data-an\]](#).